

Characterizing protein kinase A (PKA) subunits as macromolecular regulators of PKA RI α liquid–liquid phase separation

Cite as: J. Chem. Phys. 154, 221101 (2021); doi: 10.1063/5.0049810

Submitted: 9 March 2021 • Accepted: 9 May 2021 •

Published Online: 8 June 2021






View Online



Export Citation



CrossMark

Surl-Hee Ahn,¹  Sanbo Qin,^{2,3} Jason Z. Zhang,^{4,5}  J. Andrew McCammon,^{1,4}  Jin Zhang,^{4,5} and Huan-Xiang Zhou^{2,6,a)} 

AFFILIATIONS

¹Department of Chemistry and Biochemistry, University of California San Diego, La Jolla, California 92093, USA

²Department of Chemistry, University of Illinois at Chicago, Chicago, Illinois 60607, USA

³Institute of Molecular Biophysics, Florida State University, Tallahassee, Florida 32306, USA

⁴Department of Pharmacology, University of California San Diego, La Jolla, California 92093, USA

⁵Department of Bioengineering, University of California San Diego, La Jolla, California 92093, USA

⁶Department of Physics, University of Illinois at Chicago, Chicago, Illinois 60607, USA

^{a)}Author to whom correspondence should be addressed: hzhou43@uic.edu

<https://doi.org/10.1063/5.0049810>

The ubiquitous small molecule cyclic adenosine monophosphate (cAMP) controls a diverse set of cellular processes by binding and regulating several enzymes such as protein kinase A (PKA). The PKA holoenzyme consists of a dimer of regulatory subunits and a pair of catalytic (PKA_{cat}) subunits. Binding of cAMP to PKA regulatory subunits induces the release and activation of PKA_{cat}. This binding event also increases the structural disorder of the type I regulatory subunit RI α .¹ As liquid–liquid phase separation (LLPS) is driven, in part, by intrinsic disorder, the more disordered, cAMP-bound form of RI α more readily phase separates, while the more ordered, PKA_{cat}-bound form of RI α resists phase separation² (Fig. 1). By sequestering many cAMP molecules, RI α phase separation is a crucial driver for compartmentalizing cAMP; disruption of the phase-separated bodies leads to oncogenic effects. As RI α LLPS is intricately regulated by its binding partners, we aimed to explain these complex effects through computational modeling.

Previously, Ghosh, Mazarakos, and Zhou³ reported a combined experimental and computational study to define three classes of macromolecular regulators: volume-exclusion promoters, weak-attraction suppressors, and strong-attraction promoters. Volume-exclusion regulators promote LLPS by taking up volume in the bulk phase and displacing the protein molecules undergoing LLPS to form liquid droplets. Weak-attraction regulators, on the other hand,

suppress LLPS by being weakly attracted to the protein molecules undergoing LLPS and disrupting liquid droplet formation. Strong-attraction regulators (at low concentrations) promote LLPS by forming stronger attraction with the protein molecules undergoing LLPS inside liquid droplets. By comparing *in vitro* phase diagrams of RI α liquid droplet formation under various conditions shown in Ref. 2 with phase diagrams of the three macromolecular regulators shown in Ref. 3, we can categorize the different macromolecules into one of the three regulator classes. Polyethylene glycol (PEG) 4000, which was used to mimic cellular conditions for RI α in *in vitro* experiments and was shown to be necessary for liquid droplets to form, can be categorized as a volume-exclusion promoter. On the other hand, PKA_{cat} in the presence of cAMP can be categorized as a strong-attraction promoter, and PKA_{cat} bound to cAMP-free RI α can be categorized as a weak-attraction suppressor for RI α phase separation. Computationally, the phase diagrams in Ref. 3 were obtained on patchy particle models of the same size; it is thus difficult to use them for quantitative modeling of experimental systems.

To characterize the degree of attraction between different protein partners, here we developed a method called fast Fourier transform (FFT)-based Modeling of Atomistic Protein–protein interactions applied to cross second virial coefficient B_{23} (FMAPB23). FMAPB23 is an extension of FMAPB2,^{4–7} which calculates the

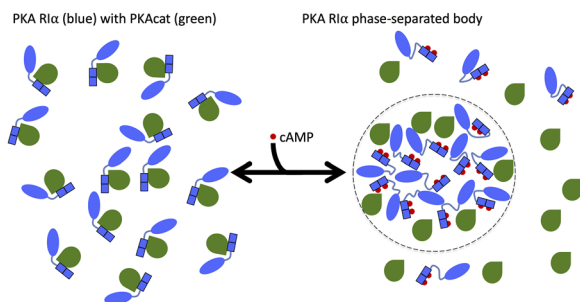


FIG. 1. Illustration of the regulation of PKA R1 α phase separation by different binding partners. Binding of two cAMP molecules (red) per R1 α subunit (blue) leads to dissociation (and activation) of PKA_{cat} (green). The increased disorder in the R1 α linker region [between the N-terminal dimerization and docking (D/D) domain in oval and tandem cAMP-binding domains in rectangle] and the action of the dissociated PKA_{cat} promote the formation of phase-separated bodies (highlighted on the right with a dotted boundary). In contrast, PKA_{cat} in the absence of cAMP suppresses R1 α phase separation by binding to and rigidifying R1 α (shown on the left). For clarity, only a half of a holoenzyme, consisting of a single PKA_{cat} subunit and a single R1 α subunit, is illustrated.

second virial coefficient B_2 for all-atom proteins in an implicit solvent. B_2 is determined by the interaction energy between two molecules of the same protein, which includes steric, electrostatic, and non-polar components. Specifically, B_2 is the integration of the Mayer f -function or $e^{-\beta U(\mathbf{R}, \Omega, X)} - 1$,

$$B_2 = -\frac{1}{2} \frac{1}{8\pi^2} \frac{1}{\mathcal{V}_X} \int d\mathbf{R} d\Omega dX \left[e^{-\beta U(\mathbf{R}, \Omega, X)} - 1 \right], \quad (1)$$

where \mathbf{R} denotes the relative position vector between the two molecules, Ω denotes three relative rotation angles, such as the Euler angles, X denotes internal degrees of freedom (in flexible molecules), $U(\mathbf{R}, \Omega, X)$ denotes the intermolecular interaction energy, and $\mathcal{V}_X = \int dX$. A potential of mean force (PMF) $W(R)$ is obtained by averaging over all but the intermolecular distance R ,

$$\begin{aligned} e^{-\beta W(R)} &\equiv \frac{1}{4\pi} \frac{1}{8\pi^2} \frac{1}{\mathcal{V}_X} \int d\theta d\phi d\Omega dX \sin \theta e^{-\beta U(\mathbf{R}, \Omega, X)} \\ &\equiv \langle e^{-\beta U(\mathbf{R}, \Omega, X)} \rangle_{\theta, \phi, \Omega, X}, \end{aligned} \quad (2)$$

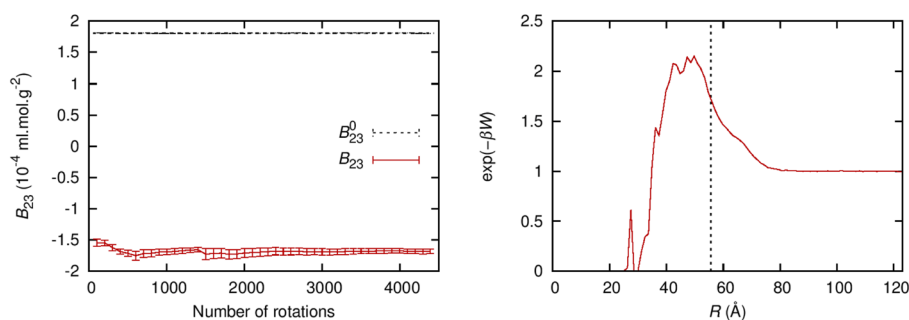
where θ and ϕ denote the polar and azimuthal angles of the relative position vector \mathbf{R} . Note that from Eq. (1), it is apparent that repulsive interactions [i.e., positive $U(\mathbf{R}, \Omega, X)$] will make B_2 more positive, whereas attractive interactions [i.e., negative $U(\mathbf{R}, \Omega, X)$] will make B_2 more negative. The terms of the interaction energy are then expressed as correlation functions and calculated by using FFT. In comparison, B_{23} is determined by the interaction energy between two **different** protein molecules. The calculations of B_2 and B_{23} are thus identical, except that the interaction energy is between two of the **same** kind of molecule for the former but between two **different** kinds of molecules for the latter. FMAPB2 has a scaling parameter (ν_s) for non-polar interactions that depends on protein molecular weight M (in kD). We took the geometrical mean of the molecular weights of the two protein molecules as M for calculating ν_s in FMAPB23.

To use FMAPB23 in practice, the program requires as input the ionic strength, temperature, and structure files of the two protein molecules in the PQR format. The PQR files can be converted using PDB2PQR⁸ from structural files downloaded from the Protein Data Bank (PDB). The atomic partial charges for protein residues are from the PARSE set.⁹ The output from FMAPB23 is similar to that of FMAPB2, which includes B_{23} , its steric component B_{23}^0 , and the PMF over distance R between the two protein molecules, as shown in Fig. 2. In calculating the steric component B_{23}^0 , the two protein molecules are assumed to only have steric repulsion, corresponding to an infinite interaction energy whenever any atom of one molecule clashes with any atom of the other molecule. As with FMAPB2,⁷ at low temperatures, B_{23} can be dominated by a few low energy configurations, potentially leading to significant errors. In addition, a grid spacing around 0.6 Å is necessary for discretization in FFT calculations in order to get converged energies, which limits how large the proteins can be for the available memory of a computer.

The cross second virial coefficient B_{23} was calculated for Mg²⁺-bound PKA_{cat} [denoted as PKA_{cat}(Mg²⁺)] and cAMP-bound R1 α [denoted as R1 α (cAMP)]. Five structures for the first molecule were taken from PDB: 6NO7 chains E and G, 3O7L chain B, and 4NTT chains A and B; two structures for the second molecule were taken from 4MX3 chains A and B. The results from the total of ten runs were used to calculate a mean value and a standard error of the mean (see Table I). Note that Mg²⁺ was taken as an integral part of molecule 1, while cAMP was taken as an integral part of molecule 2. Partial charges for Mg²⁺ and cAMP were unavailable from the PARSE set. For Mg²⁺, we assumed a charge of +2 as a crude treatment; partial charges of cAMP were obtained from the R.E.D. Server.¹⁰ B_{23} was also calculated for the PKA_{cat}(Mg²⁺)-R1 α complex and cAMP-free R1 α . The structures were from PDB: 6NO7, with chains EF or GH for molecule 1 and chains B, D, F, or H for molecule 2. We assume that PKA_{cat}(Mg²⁺) is tightly bound to R1 α in the absence of cAMP as experimental results indicate, and thus, we treat the entire complex as molecule 1. Finally, for sake of comparison, we calculated B_{23} for PKA_{cat}(Mg²⁺) and cAMP-free R1 α (see Fig. 2). The structures were the same as for the preceding set of calculations, except that molecule 1 only contained chain E or G. All R1 α structures started at residue 105 to ensure a fair comparison across the different molecular pairs; the truncated residues, including the dimerization and docking (D/D) domain and part of the linker region, were not resolved in cAMP-bound R1 α structures due to disorder.

To facilitate comparison across different molecular pairs, we normalized B_{23} by its steric component, B_{23}^0 . The latter is dictated by the molecular size. The mean of B_{23}/B_{23}^0 and standard error of the mean for each of the three molecular pairs described in the preceding paragraph are listed in Table I. All of the normalized B_{23} values are negative, with the PKA_{cat}(Mg²⁺)-R1 α complex and cAMP-free R1 α pair having the least negative value, whereas the PKA_{cat}(Mg²⁺) and R1 α (cAMP) pair having the most negative value. This contrast matches with the PKA_{cat}(Mg²⁺)-R1 α complex in the absence of cAMP being a weak-attraction suppressor and PKA_{cat}(Mg²⁺) in the presence of cAMP being a strong-attraction promoter for R1 α phase separation. Specific binding with R1 α prevents PKA_{cat}(Mg²⁺) to form strong additional interaction with R1 α , thus explaining why the PKA_{cat}(Mg²⁺)-R1 α complex is a weak-attraction suppressor of R1 α phase separation. Indeed, as measured by B_{23}/B_{23}^0 ,

Ionic Strength	Temperature	Molecular Weight A	Molecular Weight B	Net Charge A	Net Charge B	ν_s	B_{23}^0	B_{23}
(M)	(°C)	(Da)	(Da)	(e)	(e)		(10^{-4} ml.mol.g $^{-2}$)	(10^{-4} ml.mol.g $^{-2}$)
0.150	25.00	39207	30631	7	-10	0.140	1.806 ± 0.0007	-1.684 ± 0.0363



[Radial Distribution Data](#); [Residue Interaction Energy](#)

FIG. 2. Output from the FMAPB23 server for PKA_{cat}(Mg²⁺) (PDB: 6NO7 E) and RI α (PDB: 6NO7 H; with residues up to residue 104 truncated). Along with the calculated results for B_{23}^0 and B_{23} presented in a table, the output includes plots of (*left panel*) the convergence of B_{23} as a function of the number of rotations of the probe molecule and (*right panel*) the radial distribution function. The two molecules are labeled as A and B; A is static, whereas B is rotated many times (as specified by “Number of rotations”) to evaluate the integration over Ω . Error bars represent standard deviations among the different rotations. The radial distribution function is the Boltzmann factor of the potential of mean force along the distance R between the two protein molecules. The vertical dashed line in the radial distribution function plot represents the contact distance of two spheres with the same B_{23}^0 value as the two protein molecules. Links to the raw data for the radial distribution function and the residue interaction energy (“Radial Distribution Data” and “Residue Interaction Energy”) are also created on the output page.

nonspecific interactions of PKA_{cat}(Mg²⁺) alone with RI α are almost as strong as with RI α (cAMP). Had we not considered the specific binding and hence not used the entire PKA_{cat}(Mg²⁺)-RI α complex as molecule 1 in calculating B_{23} with RI α , we would have concluded PKA_{cat}(Mg²⁺) to be a strong-attraction promoter for RI α LLPS, which would have contradicted with experimental results.

We can gain further insight into the effects of intermolecular interactions on LLPS by calculating the second virial coefficient B_2 for each protein molecule using FMAPB2.⁷ B_2 results were obtained for PKA_{cat}(Mg²⁺) (6NO7 E, 6NO7 G, 3O7L B, 4NTT A, and 4NTT B), cAMP-free RI α (6BYR B, 6BYR D, 6BYS B, 6BYS D, 6BYS F, 6BYS H, 6NO7 B, 6NO7 D, 6NO7 F, and 6NO7 H), RI α (cAMP) (4MX3 A and 4MX3 B), and PKA_{cat}(Mg²⁺)-RI α complex (6NO7 EF and 6NO7 GH). The mean and standard error of the mean for the normalized B_2 value, i.e., B_2/B_2^0 , calculated from the multiple input structures for each protein are listed in Table II. Several observations can be made by comparing the normalized B_2 values against the normalized B_{23} values. First off, B_2/B_2^0 is

slightly positive for the PKA_{cat}(Mg²⁺)-RI α complex, whereas B_2/B_2^0 for either of the two subunits and B_{23}/B_{23}^0 between the subunits are negative. This contrast indicates that residues in the interface of the PKA_{cat}(Mg²⁺)-RI α complex make major contributions to the self- and cross-attraction of the subunits, thus corroborating the above statement that “specific binding with RI α prevents PKA_{cat}(Mg²⁺) to form strong additional interaction with RI α .” More importantly, it is the relative strengths between self- and cross-interactions that dictate the classification of regulator effects on LLPS.³ We propose that self- and cross-interactions are captured by B_2/B_2^0 and B_{23}/B_{23}^0 , respectively. For the phase separation of RI α (cAMP) under regulation by PKA_{cat}(Mg²⁺), the relevant B_2/B_2^0 [for RI α (cAMP)] is -0.480 , whereas the relevant B_{23}/B_{23}^0 [between PKA_{cat}(Mg²⁺) and RI α (cAMP)] is -1.002 . The latter more negative value puts PKA_{cat}(Mg²⁺) in the category of strong-attraction promoter. In contrast, for the phase separation of RI α under regulation by PKA_{cat}(Mg²⁺)-RI α , the relevant B_2/B_2^0 (for RI α) is -0.467 , whereas the relevant B_{23}/B_{23}^0

TABLE I. B_{23} results.

Molecule no. 1	Molecule no. 2	B_{23}/B_{23}^0
PKA _{cat} (Mg ²⁺)-RI α	RI α	-0.321 ± 0.038
PKA _{cat} (Mg ²⁺)	RI α (cAMP)	-1.002 ± 0.029
PKA _{cat} (Mg ²⁺)	RI α	-0.978 ± 0.031

TABLE II. B_2 results.

Molecule	B_2/B_2^0
PKA _{cat} (Mg ²⁺)	-0.583 ± 0.127
RI α	-0.467 ± 0.038
RI α (cAMP)	-0.480 ± 0.143
PKA _{cat} (Mg ²⁺)-RI α	0.078 ± 0.011

[between $\text{PKA}_{\text{cat}}(\text{Mg}^{2+})\text{-RI}\alpha$ and $\text{RI}\alpha$] is -0.321 . The latter less negative value puts $\text{PKA}_{\text{cat}}(\text{Mg}^{2+})\text{-RI}\alpha$ in the category of weak-attraction suppressor.

In addition to the final B_{23} , the intermediate results of FMAPB23 can also be used to determine residue-level decomposition of interaction energies. From the billions of intermolecular poses sampled in a typical FMAPB23 calculation, we collected the 1000 configurations with the lowest intermolecular interaction energies. The contributions of individual residues to the interaction energies were then averaged over the 1000 selected poses. The results are illustrated in Fig. 3 for the cross-interaction between $\text{PKA}_{\text{cat}}(\text{Mg}^{2+})$ and cAMP-free $\text{RI}\alpha$. Confirming the foregoing conclusion that residues in the interface of the $\text{PKA}_{\text{cat}}(\text{Mg}^{2+})\text{-RI}\alpha$ complex make major contributions to the cross attraction of the subunits, four of the top five $\text{PKA}_{\text{cat}}(\text{Mg}^{2+})$ contributors (Lys192, Arg194, Trp196, and Lys213) and three of the top five $\text{RI}\alpha$ contributors (Glu168, Tyr205, and Arg355) are interface residues. The residue-level contributions to the self-interaction energy of cAMP-free $\text{RI}\alpha$ are shown in Fig. 4. This time, all of the experimentally resolved residues in cAMP-free $\text{RI}\alpha$ are used (6BYR B, 6BYR D, 6BYS B,

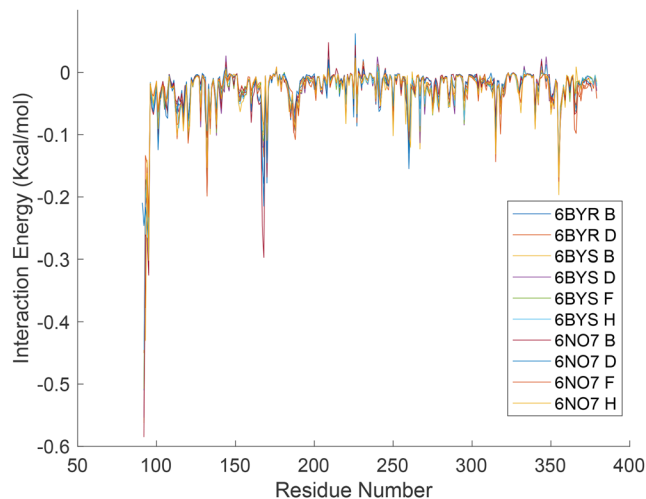
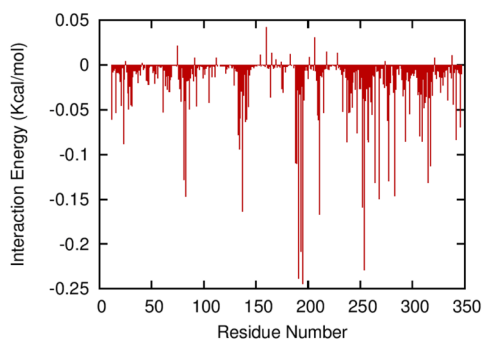


FIG. 4. Residue-level decomposition of the self-interaction energy for PKA $\text{RI}\alpha$. The legend indicates the PDB files used as input.

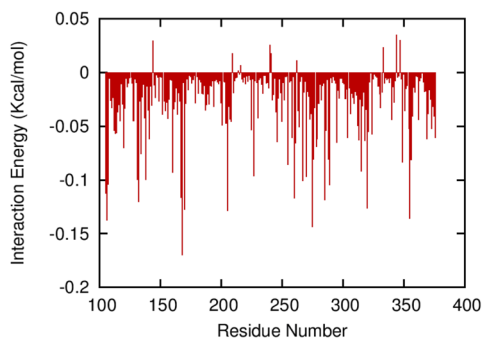
Residue Interaction Energy

subA



[Residue Interaction Energy](#); same information presented in the B-factor column of a PDB file.

subB



[Residue Interaction Energy](#); same information presented in the B-factor column of a PDB file.

FIG. 3. Residue interaction energy output from FMAPB23 for $\text{PKA}_{\text{cat}}(\text{Mg}^{2+})$ (6NO7 E; subA) and cAMP-free $\text{RI}\alpha$ (6NO7 H with residues truncated up to residue 104; subB). The results are plotted as a bar graph and also displayed on a structure, with green, yellow, and red showing small, medium, and large contributions, respectively. Links to the raw data (“Residue Interaction Energy” and “same information presented in the B-factor column of a PDB file”) are also created on the output page.

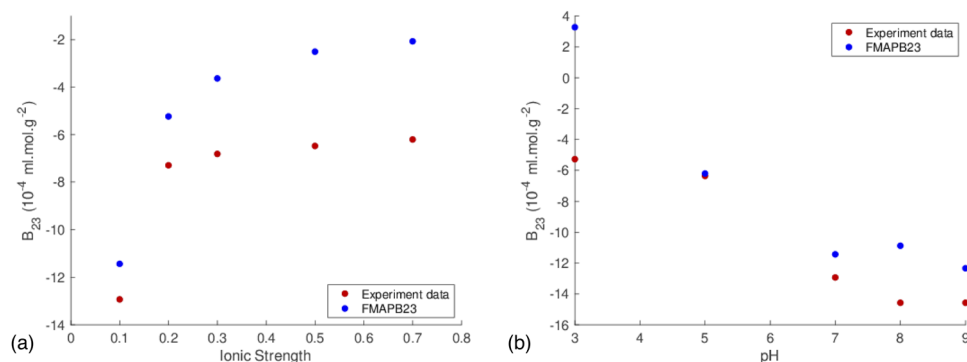


FIG. 5. Calculated B_{23} values by FMAPB23 vs experimental data for the BSA-lysozyme system. (a) B_{23} values at different ionic strengths (NaCl concentrations in M), 25 °C, and pH 7.0. (b) B_{23} values at different pHs, 25 °C, and 0.1 M NaCl concentration.

6BYS D, 6BYS F, 6BYS H, 6NO7 B, 6NO7 D, 6NO7 F, and 6NO7 H), including the linker residues before residue 105. Note that disorder-prone residues in the linker region make the greatest contributions to the RI α self-interaction energy, even more than the other interface residues (Lys132, Glu168, Trp260, and Arg355). This linker region was indeed found to be important for RI α LLPS.²

Finally, B_{23} calculated by FMAPB23 can be directly compared against experimental measurements. The calculated results for the bovine serum albumin (BSA)-lysozyme pair at different ionic strengths and at different pHs are shown in Figs. 5(a) and 5(b), respectively, along with the corresponding experimental data.¹¹ Although the calculated and experimental values do not match up exactly, the trends do match up quite well. These results showcase the utility of the FMAPB23 program to study protein-protein non-specific interactions. Importantly, our results suggest that interaction energies between RI α and PKA_{cat}, in the presence and absence of cAMP, can explain the unique properties of RI α LLPS. Overall, this study demonstrates how computational modeling can give insight into complex protein assemblies, such as phase-separated protein droplets.

FMAPB23 is available as a web server at <http://pipe.rcc.fsu.edu/fmapb23>, and FMAPB2 is available as a web server at <http://pipe.rcc.fsu.edu/fmapb2>.

S.-H.A. and S.Q. contributed equally to this work.

This work was supported by National Institutes Grant Nos. GM31749 (to J.A.M.) and GM118091 (to H.-X.Z.). The computation was performed on the clusters at the Research Computing Center of Florida State University.

DATA AVAILABILITY

The data that support the findings of this study are available from the corresponding author upon reasonable request.

REFERENCES

- 1 C. Kim, N.-H. Xuong, and S. S. Taylor, "Crystal structure of a complex between the catalytic and regulatory (RI α) subunits of PKA," *Science* **307**, 690–696 (2005).
- 2 J. Z. Zhang, T.-W. Lu, L. M. Stolerman, B. Tenner, J. R. Yang, J.-F. Zhang, M. Falcke, P. Rangamani, S. S. Taylor, S. Mehta *et al.*, "Phase separation of a PKA regulatory subunit controls cAMP compartmentation and oncogenic signaling," *Cell* **182**, 1531–1544 (2020).
- 3 A. Ghosh, K. Mazarakos, and H.-X. Zhou, "Three archetypical classes of macromolecular regulators of protein liquid-liquid phase separation," *Proc. Natl. Acad. Sci. U. S. A.* **116**, 19474–19483 (2019).
- 4 S. Qin and H.-X. Zhou, "FFT-based method for modeling protein folding and binding under crowding: Benchmarking on ellipsoidal and all-atom crowders," *J. Chem. Theory Comput.* **9**, 4633–4643 (2013).
- 5 S. Qin and H.-X. Zhou, "Further development of the FFT-based method for atomistic modeling of protein folding and binding under crowding: Optimization of accuracy and speed," *J. Chem. Theory Comput.* **10**, 2824–2835 (2014).
- 6 S. Qin and H.-X. Zhou, "Fast method for computing chemical potentials and liquid-liquid phase equilibria of macromolecular solutions," *J. Phys. Chem. B* **120**, 8164–8174 (2016).
- 7 S. Qin and H.-X. Zhou, "Calculation of second virial coefficients of atomistic proteins using fast Fourier transform," *J. Phys. Chem. B* **123**, 8203–8215 (2019).
- 8 T. J. Dolinsky, J. E. Nielsen, J. A. McCammon, and N. A. Baker, "PDB2PQR: An automated pipeline for the setup of Poisson-Boltzmann electrostatics calculations," *Nucleic Acids Res.* **32**, W665–W667 (2004).
- 9 D. Sitkoff, K. A. Sharp, and B. Honig, "Accurate calculation of hydration free energies using macroscopic solvent models," *J. Phys. Chem.* **98**, 1978–1988 (1994).
- 10 E. Vanquelef, S. Simon, G. Marquant, E. Garcia, G. Klimmerak, J. C. Delepine, P. Cieplak, and F.-Y. Dupradeau, "R.E.D. Server: A web service for deriving RESP and ESP charges and building force field libraries for new molecules and molecular fragments," *Nucleic Acids Res.* **39**, W511–W517 (2011).
- 11 S. H. Choi and Y. C. Bae, "Osmotic cross second virial coefficient (B_{23}) of unfavorable proteins: Modified Lennard-Jones potential," *Macromol. Res.* **17**, 763–769 (2009).